MATERIALS SCIENCE

Ultra-large electric field–induced strain in potassium sodium niobate crystals

Chengpeng Hu[1]*, Xiangda Meng[1]*, Mao-Hua Zhang[2]*, Hao Tian[1†], John E. Daniels[3], Peng Tan[1], Fei Huang[1], Li Li[4], Ke Wang[2†], Jing-Feng Li[2], Qieni Lu[5], Wenwu Cao[6,7], Zhongxiang Zhou[1†]

Electromechanical coupling in piezoelectric materials allows direct conversion of electrical energy into mechanical energy and vice versa. Here, we demonstrate lead-free (K_xNa_{1-x})NbO_3 single crystals with an ultrahigh large-signal piezoelectric coefficient d_{33}* of 9000 pm V^{-1}, which is superior to the highest value reported in state-of-the-art lead-based single crystals (~2500 pm V^{-1}). The enhanced electromechanical properties in our crystals are realized by an engineered compositional gradient in the as-grown crystal, allowing notable reversible non-180° domain wall motion. Moreover, our crystals exhibit temperature-insensitive strain performance within the temperature range of 25°C to 125°C. The enhanced temperature stability of the response also allows the materials to be used in a wider range of applications that exceed the temperature limits of current lead-based piezoelectric crystals.

INTRODUCTION

Perovskite ferroelectrics with a coupling among the polarization, strain and electric field, have found extensive applications in the fields of information and communication, medical imaging, and diagnosis. Because of their ease of processing and low cost, piezoceramics dominate the market. The piezoresponse of polycrystalline piezoceramics is an ensemble average of the piezoelectric response over all possible crystallographic orientations of the corresponding single crystal. The mutual clamping of the neighboring grains associated with the polycrystalline ceramic hinders their property magnitudes. This clamping is the main reason why the electric field–induced strain of piezoceramics has generally failed to exceed a value of 1.0% (*1*, *2*). Ferroelectric single crystals, wherein the piezoelectricity can be tailored by orienting the crystal in an optimal direction, are of great interest because of their superior piezoelectric coupling and dielectric properties (*3*–*7*). Of particular importance are the lead-based relaxor ferroelectric single crystals $(1-x)Pb(Mg_{1/3}Nb_{2/3})O_3$-$xPbTiO_3$ (PMN-xPT) and $(1-x)Pb(Zn_{1/3}Nb_{2/3})O_3$-$xPbTiO_3$ (PZN-xPT). These materials readily exhibit a large strain of 1.7% at an electric field of 12 kV mm^{-1}, giving out an ultrahigh piezoelectric constant (d_{33}* = 2500 pm V^{-1}). This material advancement facilitates the development of electromechanical devices, with growing investment in crystal growth technologies to maximize the yield and lower the costs. While PMN-xPT and PZN-xPT single crystals are now state of the art in high-end applications such as ultrasonic medical imaging and naval sonar, they have a limited future in consumer devices due to environmental regulations limiting the use of lead (*8*). This has driven an increasing research trend toward developing lead-free–based materials (*9*–*13*).

The ferroelectric single crystals PMN-xPT and PZN-xPT usually display enhanced piezoelectricity when the composition approaches the morphotropic phase boundary (MPB), whereby a facilitated variation in the polarization (*14*, *15*) and strain occurs under an electrical excitation. Another important characteristic of these relaxor-based ferroelectric single crystals is the presence of polar nanoregions (PNRs), which contribute to 50 to 80% of the dielectric and piezoelectric properties (*16*). In addition to the inherent mechanisms associated with the MPB and PNRs, alternative approaches include an engineered domain configuration (*3*, *17*–*20*) and defect-mediated domain switching (*21*) to enhance the piezoelectric response. However, there is a limit on the piezoelectric properties that can be achieved in PMN-xPT and PZN-xPT single crystals on the basis of the abovementioned mechanisms and methods.

In this work, we propose to take advantage of an engineered compositional gradient to further increase the contribution of domain wall motion in lead-free–based ferroelectric (K_xNa_{1-x})NbO_3 (KNN) single crystals. An ultra-large large-signal piezoelectric constant d_{33}* of 9000 pm V^{-1} under a relatively small electric field of 1 kV mm^{-1} is obtained. The response is at least three times larger than that of PMN-xPT single crystals under the same electrical stimulus. Moreover, temperature-insensitive electric field–induced strain performance is observed within the temperature range of 25°C to 125°C due to a high Curie temperature of 420°C.

RESULTS AND DISCUSSION

The ultra-large piezoelectric properties

An ultra-large strain of 0.9% and an unprecedented d_{33}* of 9000 pm V^{-1} at an electric field of 1 kV mm^{-1} are found for $K_{0.43}Na_{0.57}NbO_3$ single crystals (KNN43), as shown in Fig. 1A. Representative lead-based crystals were also compared (*3*, *6*). The high large-signal piezoelectric coefficient d_{33}* is at least three times the value of the relaxor-PT crystals. The strain response was confirmed on KNN43 samples from repeated crystal growths, and also by Mach-Zehnder digital holographic interferometry, which shows consistent results with strains measured by a traditional laser interferometer (fig. S3). The temperature dependence of the d_{33}* values is shown in Fig. 1B, which exhibits superior thermal stability to that of PZN-6.5PT (*22*) and PMN-33PT crystals (fig. S4), owing to a high Curie temperature

---

[1] Department of Physics, Harbin Institute of Technology, Harbin 150001, P. R. China. [2] State Key Laboratory of New Ceramics and Fine Processing, School of Materials Science and Engineering, Tsinghua University, Beijing 100084, P. R. China. [3] School of Materials Science and Engineering, UNSW Australia, Sydney, NSW 2052, Australia. [4] Key Laboratory of In-Fiber Integrated Optics of Ministry of Education, College of Science, Harbin Engineering University, Harbin 150001, P. R. China. [5] College of Precision Instruments and Optoelectronics Engineering, Tianjin University, Tianjin 300072, P. R. China. [6] Condensed Matter Science and Technology Institute, Harbin Institute of Technology, Harbin 150001, P. R. China. [7] Materials Research Institute, The Pennsylvania State University, University Park, PA 16802, USA.
*These authors contributed equally to this work.
†Corresponding author. Email: tianhao@hit.edu.cn (H.T.); wang-ke@tsinghua.edu.cn (K.W.); zhouzx@hit.edu.cn (Z.Z.)

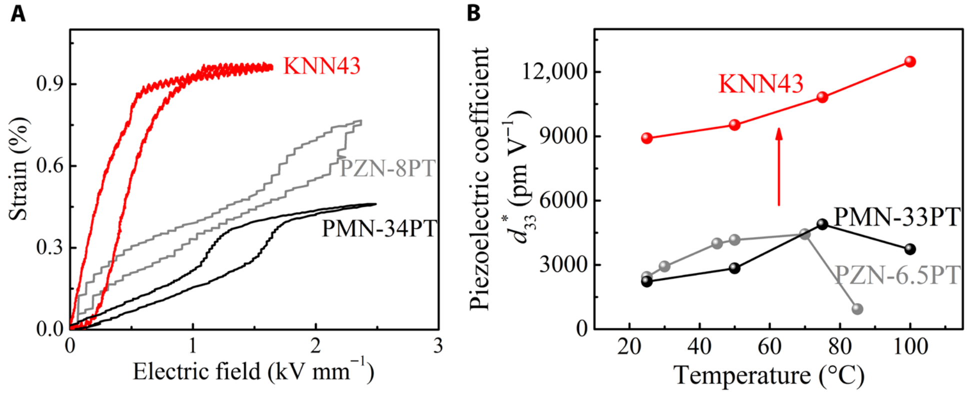

Fig. 1. Piezoelectric response for the KNN43 crystal. (**A**) Room temperature comparison of the electric field–induced strain obtained in this work with that for other materials with a relatively high strain. (**B**) Comparison of d_{33}* values at different temperatures. The unipolar measurement was performed along the [001] pseudo-cubic direction at a frequency of 1 Hz.

of 420°C (fig. S5). With increasing temperature, the value of d_{33}* increases slightly from 9000 to 9900 pm V^{-1} at 75°C. The strain behavior was recorded from room temperature to 125°C (fig. S6), exhibiting not only high strain performance but also little variation over the temperature range. Notably, the temperature-dependent strains were obtained under a reduced driving field of 0.5 kV mm^{-1}, which is significantly less than that required for conventional polycrystalline piezoelectric materials (4 kV mm^{-1} or more). The large-signal piezoelectric coefficient d_{33}* value is two orders of magnitude larger than the small signal d_{33} of 190 pC N^{-1} measured using the Berlincourt method. This implies that the large-signal response is possibly due to reversible domain switching that is not active under low stresses.

Structural mechanism

The mechanism of strain was demonstrated by performing in situ high-energy x-ray scattering experiments. Here, a segment of a three-dimensional reciprocal space map covering the reciprocal lattice units of approximately $0 < hkl < 4.5$ was collected. Figure 2A shows the *hk* and *hl* reciprocal lattice planes from this volume that are aligned perpendicular and parallel to the applied electric field vector, respectively. In this orientation, ferroelastic domain structures are observed by splitting the parent cubic phase reflections. Figure 2 (B and D) shows that, in the initial state, the crystal displays ferroelastic domains in the *hk* plane (perpendicular to the field) but not in the *hl* plane (parallel to the field). With the application of an electric field of 1.2 kV mm^{-1} (Fig. 2, C and E), additional diffraction spots appear in the *hl* plane at lower *q*-vector magnitudes than the initial state. This finding indicates the nucleation of domains with their maximum spontaneous strain direction and thus polar direction parallel to the applied field vector. The reciprocal space maps were collected in 0.2 kV mm^{-1} steps from the initial state to 1.2 kV mm^{-1}. Summed line scans along the reciprocal lattice line of 31*l* are shown in fig. S7. Here, domain nucleation begins after 0.2 kV mm^{-1} and develops rapidly between 0.4 and 0.6 kV mm^{-1}.

Small signal d_{33} along the compositional gradient

Because this phenomenon was only observed in a select region of a large crystal boule, extensive experiments were carried out across the compositional gradient within the boule to understand the origin. A plot of the direct piezoelectric coefficient d_{33} (using the Berlincourt method, different from the large-signal d_{33}* obtained by strain versus electric field) as a function of the potassium content, *x*, in the range of $x = 0.2$ to 0.8 is shown in Fig. 3A (the testing details are provided in the Supplementary Materials). The crystals were sliced perpendicular to the crystal growth direction $[001]_C$, and the samples were placed with the lower potassium content side upward, as shown in Fig. 3B. Notably, the KNN crystals exhibit d_{33} values without poling. The "As-grown" line shows that the d_{33} values are negative in regions I and II and positive in regions IV and V. The opposite piezoelectric coefficients indicate different orientations of a change in the spontaneous polarization with small stress values, which are upward and downward for regions I and II and regions IV and V, respectively. The macroscopic spontaneous polarization, in which the direction is the same as d_{33}, is also confirmed by the difference between the positive and negative coercive biases, i.e., the imprint, acquired from the polarization-electric (*P-E*) hysteresis (fig. S9). While most of the polarization vectors in region III lie in a plane, the crystals exhibit relatively small d_{33} values, likely due to the coexistence of upward and downward macroscopic spontaneous polarizations. The crystals with different potassium content are endowed with three different polarization vector configurations, as illustrated in Fig. 3C. Moreover, it is obvious that the d_{33} negative peak is located in region II. Here, the d_{33} transitions rapidly through zero as the composition changes only slightly toward region III, indicating that the polarization direction is highly frustrated between opposing directions. It is in this transition region where we propose that the maximum in large-signal piezoelectric response is observed.

Domain structure versus composition change

Excellent piezoelectric properties are always accompanied by particular domain structures. Notably, different regions in the current KNN crystal boule show distinct domain configurations (as shown in Fig. 3, D to F; for more details, see fig. S11). Large stripe domains were obtained in region I, where relatively small d_{33} values are observed. In region II, large domains are absent and replaced by smaller herringbone domains. Then, the herringbone domains disappear, while the labyrinthine domains appear in region III. Miniaturized domain structures are common in ferroelectrics near the MPB, which is associated with a decrease in the crystallographic anisotropy of the polarization vector directions (*23*).

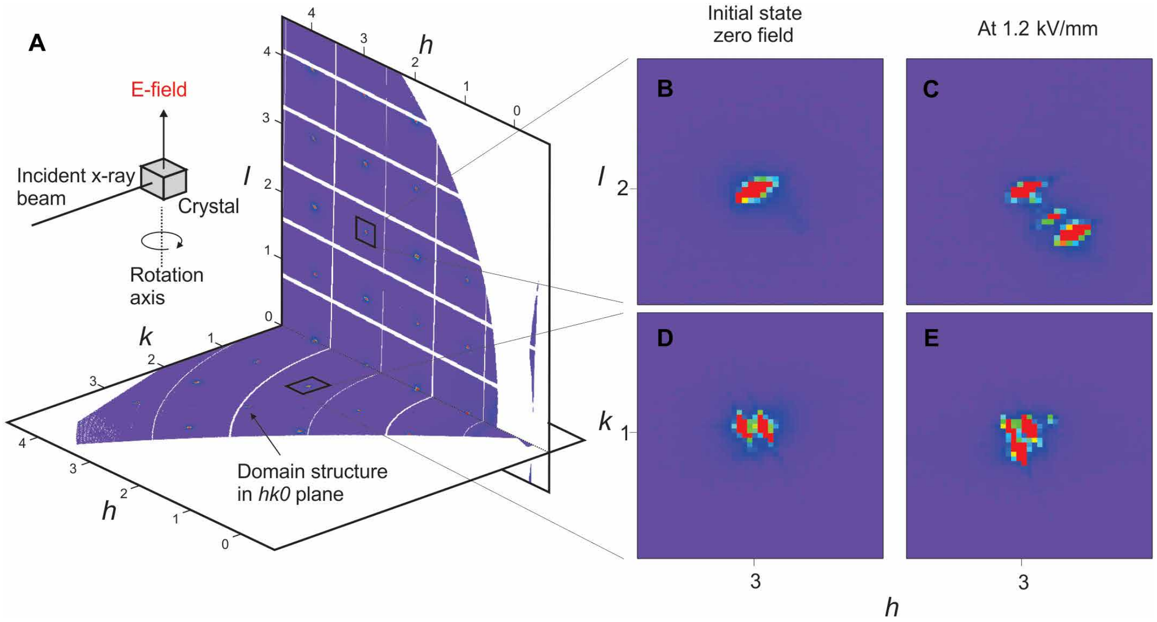

Fig. 2. In situ reciprocal space mapping of the crystal. (**A**) Schematic representation of the data collection geometry and cut-away *hk* and *hl* planes from the reciprocal space volume in the initial state: (**B** and **C**) 302 diffraction peaks before and after the application of the electric field and (**D** and **E**) 310 diffraction peaks before and after the application of the electric field.

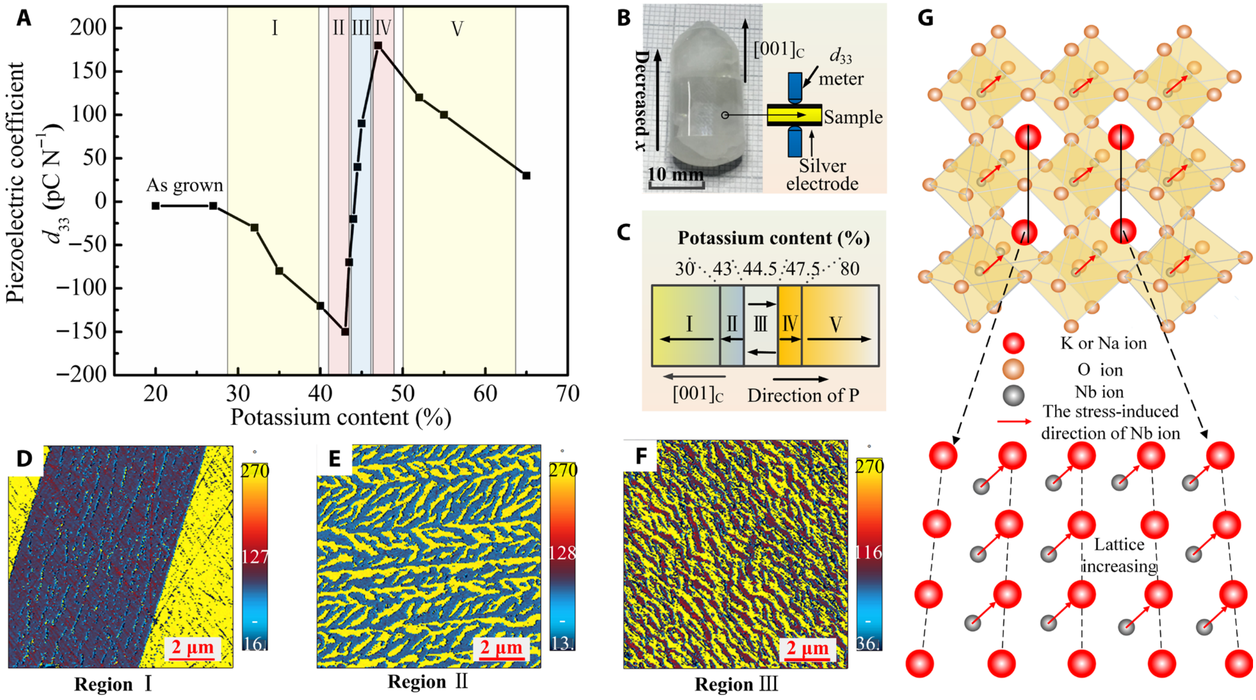

Fig. 3. Piezoelectric coefficient and domain structures of the KNN crystals. (**A**) Piezoelectric coefficient d_{33} as a function of the potassium content. Regions I to V indicate areas where the potassium content *x* is 0.29 to 0.40, 0.41 to 0.43, 0.43 to 0.46, 0.46 to 0.48, and >0.5, respectively. (**B**) KNN crystal grown via the top-seeded solution-growth method. All samples were polished to a thickness of 0.2 mm. (**C**) Schematic diagram of the polarization direction with composition changes before poling. The directions of P in the schematic diagram only represent the projection of the macro-spontaneous polarization in the $[001]_C$ direction while ignoring the other directions. Domain configurations under a piezoelectric force microscope at *x* values of (**D**) 0.37, (**E**) 0.43, and (**F**) 0.45. (**G**) Schematic diagram of the compositional gradient–induced stress that generates a restoring force.

When ferroelectrics are subjected to an electric field, the domains align themselves along the direction of the electric field, giving rise to a macroscopic strain. After poling, some domains remain oriented along the electric field direction, and others are reversed or switched back to their initial state. However, if there is a driving force to reverse all of the domains perpendicular to the applied field direction, then a mechanism of ultra-high electric field–induced strain is accessed. The record-high electric field–induced strain reported here is shown by in situ diffraction to be due to this large volume fraction of switchable domains. Previous studies have suggested that point defect–pinned domains (*21*) and substrate-clamped domains (*24*–*27*) can be used to facilitate this reversible domain switching and, in turn, the high level of strain. It is proposed that in the current study, this reversibility is a result of the engineered compositional gradient. Because of the presence of the compositional gradient, a variation in lattice constants along the direction of the gradient arises (see Fig. 3G). It is the compositional gradient–induced stress that generates a restoring force (see fig. S13) to facilitate reversible domain switching and consequently a large electric field–induced strain. The presence of compositional gradient is essential to the large strain, but the large strain can only be observed in the composition that is close to $K_{0.43}Na_{0.57}NbO_3$. The enhanced strain is an accumulative effect that resulted from the local stress induced by the compositional gradient that is maximum in this very composition.

In summary, an ultrahigh electric field–induced strain of 0.9% under an electric field of 1 kV mm^{-1} is achieved in lead-free ferroelectric crystal with an engineered compositional gradient. In situ x-ray diffraction (XRD) was used to demonstrate that this strain is the result of domain switching. Our discovery in this work indicates tremendous opportunities for the development of high-performance piezoelectrics from compositional gradient engineering and opens prospects for new strategies to improve electric field–induced strains in functional materials.

MATERIALS AND METHODS

Crystal growth and sample preparation

The potassium sodium niobate ($K_xNa_{1-x}NbO_3$) crystals were grown via the top-seeded solution-growth method with K_2CO_3 (99.99%), Na_2CO_3 (99.99%), and Nb_2O_5 (99.99%) powders, in which a 10 mole percent excess of Na_2CO_3 and K_2CO_3 is added as a self-flux to reduce the growth temperature. The heating system is a medium-frequency induction furnace at a frequency of 2 kHz under air atmosphere, in which the temperature was controlled by a Eurotherm 818 controller (Eurotherm, Sussex, UK) with an accuracy of ±0.3°C. The raw materials were synthesized at 900°C for 6 hours and melted at 1230°C for 6 hours. The speed of rotating and pulling the crystal was approximately 20 rpm and 4.0 mm per day, respectively. The orientations of the samples were determined by means of a Laue x-ray machine. The electrodes were pasted onto the $(001)_C$ of the samples with sizes of approximately 2 mm × 2 mm × 0.2 mm (length × width × thickness). The composition of crystals was investigated using an electron probe microanalyzer (EPMA-1720, Shimadzu, Japan). The EPMA data of three representative compositions $K_{0.41}Na_{0.59}NbO_3$, $K_{0.43}Na_{0.57}NbO_3$, and $K_{0.44}Na_{0.56}NbO_3$ are listed in tables S3 to S5.

Electrical measurements

The piezoelectric constant d_{33} was measured by a commercial piezometer Zj-5A d_{33} meter (Institute of Acoustics, Chinese Academy of Sciences, China) using the "quasi-static" method (also known as the Berlincourt method, different from the large-signal d_{33}* measured by strain versus electric field). The sample crystal was settled between two metal claws that applied a small oscillating force. The measurement procedure was as follows: The top side was on the sample surface with a lower K element content. All sample crystals were measured at least five different points, and the d_{33} value is the average value of the measured data. Two batches of samples were used to ensure that the d_{33} value was correctly measured.

The dielectric constant was measured using an impedance-capacitance-resistance (LCR) meter (E4980A, Agilent Technologies, USA) by applying an AC voltage of 1 V at frequencies of 1, 10, and 100 kHz (fig. S5).

The polarization-electric (*P-E*) field hysteresis loops (fig. S9) and electrostrain hysteresis loops were characterized using a ferroelectric test system (Precision Premier II, Radiant Technology Inc., USA and aixACCT TF Analyzer 1000, Germany). The frequencies of the *P-E* field hysteresis loops and electro-strain hysteresis loops are 100 and 1 Hz, respectively. The strain versus electric field for $K_{0.35}Na_{0.65}NbO_3$ and $K_{0.44}Na_{0.56}NbO_3$ crystals was measured for comparison (fig. S10).

Domain observation

The domain configuration was studied using piezoresponse force microscopy (PFM; Cypher, Asylum Research, USA; shown in fig. S11) and polarizing light microscopy (PLM; Axioskop 40 Pol/40A Pol, Zeiss, Germany; shown in fig. S12). PFM observations were performed with a NanoWorld Arrow EFM-50 type probe, and the cantilever spring constant is 2.8 N m^{-1} (resonance frequency, 75 kHz). The probe was equipped with a Si tip with an apex radius of 33 nm and a 5/25-nm-thick double layer of chromium and platinum/iridium (Pt/Ir) on both sides, resulting in a tip curvature radius of less than 10 nm. An amplitude of 0.5 V was applied to the conductive PFM tip, and the images were attained at a rate of 1 Hz. All of the samples polished by a diamond spray polishing agent before PFM measure-1ment were annealed at 400°C for 2 hours afterward.

Spatial strain distribution by the Mach-Zehnder system

The spatial strain distribution was confirmed with an optical method of Mach-Zehnder digital holographic interferometry, as shown in fig. S2. A He-Ne laser (Thorlabs HNL050L) pumped a linear polarized light with wavelength of 632.8 nm, which was expanded, filtered, and collimated to serve as the probe light. The horizontally linearly polarized light (named p-polarized light) through the polarizing beam splitter (PBS), reflected by the mirror M_1 and beam splitter (BS), was the reference wave. The vertically linearly polarized light (named s-polarized light), which is reflected by the PBS and then going through the BS, was the object wave. For the purpose of permitting selection of p-polarized light or s-polarized light, a half-wave plate ($\lambda/2$, here $\lambda = 632.8$ nm) was settled either in the object arm or in the reference arm. Last, the interference pattern interfering with the reference wave and object wave was recorded on a charge-coupled device (CCD). The CCD was a 14-bit digital camera (GRAS-14S5 M/C) with 1384 × 1036 pixels and a pixel size of 6.45 μm × 6.45 μm.

XRD diffraction

Single-crystal diffraction experiments were carried out at beamline ID31 of the European Synchrotron Radiation Facility. An x-ray beam energy of 68.37 keV was used in a transmission geometry. A 300-μm beam in a 1-mm cross section was used. In this case, the beam penetrates through the thickness of the crystal, and scattering information is from the bulk of the material. In our case, the crystal size was 1 mm × 1 mm × 1 mm, while the incident x-ray beam size was approximately 0.2 mm × 0.3 mm. The volume of the crystal sampled by the x-ray beam during the crystal rotation and collection of the reciprocal space maps was thus of the order of one-fifth of the full crystal volume. A Pilatus CdTe 2M detector was placed at a distance of 921 mm from the sample to collect scattering information. The sample was placed in an electric field cell and immersed in silicon oil, as shown in fig. S8. The voltage was applied in steps of 200 V mm^{-1} to a maximum field strength of 1.2 kV mm^{-1}. At each field application, the sample was rotated around the vertical axis with diffraction images integrated over 0.1° of rotation for 110°. The crystal lattice parameters were obtained with the assistance of reciprocal space mapping (shown in fig. S14), which was analyzed by a four-circle x-ray diffractometer (Rigaku SmartLab). The lattice parameters of the KNN crystals are listed in table S1.

SUPPLEMENTARY MATERIALS

Supplementary material for this article is available at http://advances.sciencemag.org/cgi/content/full/6/13/eaay5979/DC1

Supplementary Text
Fig. S1. Strain versus electric field curves.
Fig. S2. Mach-Zehnder system.
Fig. S3. Images of the spatial strain distribution.
Fig. S4. Strain versus electric field curves.
Fig. S5. Dielectric properties.
Fig. S6. Temperature dependence of unipolar strain.
Fig. S7. Development of the long-axis domains parallel to the field direction.
Fig. S8. Single crystal of KNN mounted in an electric field cell.
Fig. S9. Hysteresis loops of the KNN43 crystals.
Fig. S10. Strain versus electric field curves.
Fig. S11. Vertical PFM images of the domains.
Fig. S12. The domain configuration of the KNN single crystals by using PLM.
Fig. S13. Phase-voltage hysteresis loop of the $K_{0.37}Na_{0.63}NbO_3$ single crystal by PFM.
Fig. S14. Reciprocal space maps for the KNN single crystals.
Table S1. Lattice parameter ratio *c*/*a* of the KNN crystals.
Table S2. Properties of the KNN43 crystal.
Table S3. Measured elemental composition of $K_{0.41}Na_{0.59}NbO_3$ single crystal.
Table S4. Measured elemental composition of $K_{0.43}Na_{0.57}NbO_3$ single crystal.
Table S5. Measured elemental composition of $K_{0.44}Na_{0.56}NbO_3$ single crystal.

REFERENCES AND NOTES

1. X. Liu, X. Tan, Giant strains in non-textured $(Bi_{1/2}Na_{1/2})TiO_3$-based lead-free ceramics. *Adv. Mater.* **28**, 574–578 (2016).
2. B. Narayan, J. S. Malhotra, R. Pandey, K. Yaddanapudi, P. Nukala, B. Dkhil, A. Senyshyn, R. Ranjan, Electrostrain in excess of 1% in polycrystalline piezoelectrics. *Nat. Mater.* **17**, 427–431 (2018).
3. S. E. Park, T. R. Shrout, Ultrahigh strain and piezoelectric behavior in relaxor based ferroelectric single crystals. *J. Appl. Phys.* **82**, 1804–1811 (1997).
4. S. Zhang, F. Li, X. Jiang, J. Kim, J. Luo, X. Geng, Advantages and challenges of relaxor-$PbTiO_3$ ferroelectric crystals for electroacoustic transducers—A review. *Prog. Mater. Sci.* **68**, 1–66 (2015).
5. E. Sun, W. Cao, Relaxor-based ferroelectric single crystals: Growth, domain engineering, characterization and applications. *Prog. Mater. Sci.* **65**, 124–210 (2014).
6. S. Zhang, F. Li, High performance ferroelectric relaxor-$PbTiO_3$ single crystals: Status and perspective. *J. Appl. Phys.* **111**, 031301 (2012).
7. J. Kuwata, K. Uchino, S. Nomura, Dielectric and piezoelectric properties of 0.91Pb$(Zn_{1/3}Nb_{2/3})O_3$-0.09$PbTiO_3$ single crystals. *Jpn. J. Appl. Phys.* **21**, 1298–1302 (1982).
8. EU-Directive 2011/65/EC: Restriction of the use of certain hazardous substances in electrical and electronic equipment (RoHS). *Off. J. Eur. Union* **54**, 88–110 (2011).
9. Y. Saito, H. Takao, T. Tani, T. Nonoyama, K. Takatori, T. Homma, T. Nagaya, M. Nakamura, Lead-free piezoceramics. *Nature* **432**, 84–87 (2004).
10. Y. M. You, W.-Q. Liao, D. Zhao, H. Y. Ye, Y. Zhang, Q. Zhou, X. Niu, J. Wang, P.-F. Li, D.-W. Fu, Z. Wang, S. Gao, K. Yang, J.-M. Liu, J. Li, Y. Yan, R. G. Xiong, An organic-inorganic perovskite ferroelectric with large piezoelectric response. *Science* **357**, 306–309 (2017).
11. J. Rödel, K. G. Webber, R. Dittmer, W. Jo, M. Kimura, D. Damjanovic, Transferring lead-free piezoelectric ceramics into application. *J. Eur. Ceram. Soc.* **35**, 1659–1681 (2015).
12. J. Koruza, A. J. Bell, T. Frömling, K. G. Webber, K. Wang, J. Rödel, Requirements for the transfer of lead-free piezoceramics into application. *J. Materiomics* **4**, 13–26 (2018).
13. J. Rödel, W. Jo, K. T. Seifert, E. M. Anton, T. Granzow, D. Damjanovic, Perspective on the development of lead-free piezoceramics. *J. Am. Ceram. Soc.* **92**, 1153–1177 (2009).
14. H. X. Fu, R. E. Cohen, Polarization rotation mechanism for ultrahigh electromechanical response in single-crystal piezoelectrics. *Nature* **403**, 281–283 (2000).
15. Z. Kutnjak, J. Petzelt, R. Blinc, The giant electromechanical response in ferroelectric relaxors as a critical phenomenon. *Nature* **441**, 956–959 (2006).
16. F. Li, S. Zhang, T. Yang, Z. Xu, N. Zhang, G. Liu, J. Wang, J. Wang, Z. Cheng, Z.-G. Ye, J. Luo, T. R. Shrout, L.-Q. Chen, The origin of ultrahigh piezoelectricity in relaxor-ferroelectric solid solution crystals. *Nat. Commun.* **7**, 13807 (2016).
17. G. Xu, J. Wen, C. Stock, P. M. Gehring, Phase instability induced by polar nanoregions in a relaxor ferroelectric system. *Nat. Mater.* **7**, 562–566 (2008).
18. S. E. Park, S. Wada, L. E. Cross, T. R. Shrout, Crystallographically engineered $BaTiO_3$ single crystals for high-performance piezoelectrics. *J. Appl. Phys.* **86**, 2746–2750 (1999).
19. S. Wada, S. Suzuki, T. Noma, T. Suzuki, M. Osada, M. Kakihana, S. E. Park, L. E. Cross, T. R. Shrout, Enhanced piezoelectric property of barium titanate single crystals with engineered domain configurations. *J. Appl. Phys.* **38**, 5505–5511 (1999).
20. S. Wada, S. E. Park, L. E. Cross, T. R. Shrout, Engineered domain configuration in rhombohedral PZN-PT single crystals and their ferroelectric related properties. *Ferroelectrics* **221**, 147–155 (1999).
21. X. Ren, Large electric-field-induced strain in ferroelectric crystals by point-defect-mediated reversible domain switching. *Nat. Mater.* **3**, 91–94 (2004).
22. M. Davis, D. Damjanovic, N. Setter, Electric-field-, temperature-, and stress-induced phase transitions in relaxor ferroelectric single crystals. *Phys. Rev. B* **73**, 014115 (2006).
23. Y. M. Jin, Y. U. Wang, A. G. Khachaturyan, J. F. Li, D. Viehland, Conformal miniaturization of domains with low domain-wall energy: Monoclinic ferroelectric states near the morphotropic phase boundaries. *Phys. Rev. Lett.* **91**, 197601 (2003).
24. G. Catalan, A. Lubk, A. H. G. Vlooswijk, E. Snoeck, C. Magen, A. Janssens, G. Rispens, G. Rijnders, D. H. A. Blank, B. Noheda, Flexoelectric rotation of polarization in ferroelectric thin films. *Nat. Mater.* **10**, 963–967 (2011).
25. J. Wang, J. B. Neaton, H. Zheng, V. Nagarajan, S. B. Ogale, B. Liu, D. Viehland, V. Vaithyanathan, D. G. Schlom, U. V. Waghmare, N. A. Spaldin, K. M. Rabe, M. Wuttig, R. Ramesh, Epitaxial $BiFeO_3$ multiferroic thin film heterostructures. *Science* **299**, 1719–1722 (2003).
26. R. J. Zeches, M. D. Rossell, J. X. Zhang, A. J. Hatt, Q. He, C.-H. Yang, A. Kumar, C. H. Wang, A. Melville, C. Adamo, G. Sheng, Y.-H. Chu, J. F. Ihlefeld, R. Erni, C. Ederer, V. Gopalan, L. Q. Chen, D. G. Schlom, N. A. Spaldin, L. W. Martin, R. Ramesh, A strain-driven morphotropic phase boundary in $BiFeO_3$. *Science* **326**, 977–980 (2009).
27. J. C. Agar, A. R. Damodaran, M. B. Okatan, J. Kacher, C. Gammer, R. K. Vasudevan, S. Pandya, L. R. Dedon, R. V. K. Mangalam, G. A. Velarde, S. Jesse, N. Balke, A. M. Minor, S. V. Kalinin, L. W. Martin, Highly mobile ferroelastic domain walls in compositionally graded ferroelectric thin films. *Nat. Mater.* **15**, 549–556 (2016).

Acknowledgments: We thank the Laboratory of Micro-Optics and Photonic Technology of Heilongjiang Province for helping with the experiments. **Funding:** This work was supported by the National Natural Science Foundation of China (grant nos. 11674079, 51802055, and 51822206). **Author contributions:** C.H., J.E.D., H.T., and K.W. conceived the idea. C.H., H.T., J.E.D., L.L., and K.W. designed the experiments. Z.Z., K.W., Q.L., and W.C. provided the crystal growth and characterization devices. C.H., M.-H.Z., J.E.D., K.W., and H.T. performed and analyzed the experiments. C.H., X.M., F.H., and H.T. grew the crystals. C.H. and H.T. characterized the domain structure, *P-E* loops, and piezoelectricity. J.E.D., C.H., M.-H.Z., J.-F.L., and K.W. provided and analyzed the XRD diffraction data. X.M. and P.T. measured the spatial strain distribution by the Mach-Zehnder system. The paper was written and the figures were prepared by C.H., M.-H.Z., H.T., J.E.D., and K.W. **Competing interests:** The authors declare that they have no competing interests. **Data and materials availability:** All data needed to evaluate the conclusions in the paper are present in the paper and/or the Supplementary Materials. Additional data related to this paper may be requested from the authors.

Submitted 2 July 2019
Accepted 3 January 2020
Published 27 March 2020
10.1126/sciadv.aay5979

Citation: C. Hu, X. Meng, M.-H. Zhang, H. Tian, J. E. Daniels, P. Tan, F. Huang, L. Li, K. Wang, J.-F. Li, Q. Lu, W. Cao, Z. Zhou, Ultra-large electric field–induced strain in potassium sodium niobate crystals. *Sci. Adv.* **6**, eaay5979 (2020).